Radial Basis Function-Based Super-Twisting Sliding Mode Current Control for Single-Phase Grid-Tied Inverters

Nhat Tung Nguyen
Faculty of Electrical and Electronics Engineering, Thuyloi University, Hanoi, Vietnam
tungnn@tlu.edu.vn (corresponding author)

Thi Mai Hoang
Faculty of Electrical and Electronics Engineering, Thuyloi University, Hanoi, Vietnam
maiht@tlu.edu.vn

Duc Thinh Le
Faculty of Electrical and Electronics Engineering, Thuyloi University, Hanoi, Vietnam
thinhld@tlu.edu.vn

Received: 26 March 2026 | Revised: 5 May 2026, 12 May 2026, and 19 May 2026 | Accepted: 20 May 2026

DOI: https://doi.org/10.48084/etasr.18936

ABSTRACT

This paper proposes a current control strategy for a single-phase grid-tied inverter under conditions of parameter uncertainty and disturbance. Inductance and filter resistance deviations degrade the performance of traditional model-based control methods. To overcome this, a Radial Basis Function (RBF) neural network is used as an online observer to approximate and compensate for aggregate errors due to uncertainty and unmodeled dynamics. Simultaneously, Super-Twisting Sliding Mode Control (STSMC) is applied to reduce the chattering phenomenon and ensure finite-time convergence with a continuous control signal. The RBF–STSMC combination reduces conservatism in parameter selection and enhances system robustness. Stability is demonstrated using Lyapunov, and MATLAB/Simulink simulation results show superior performance compared to traditional SMC and PID controllers.

Keywords-single-phase grid-tied inverter; Super-Twisting Sliding Mode Control (STSMC); advanced sliding mode control; Radial Basis Function (RBF) neural network; Lyapunov stability

I. INTRODUCTION

In recent years, the rapid increase of Distributed Generation (DG) sources, especially renewable energy, has promoted the development of advanced grid-support functionalities in power converters [1]. Such functionalities improve system resilience under faults and grid disturbances and typically include low/high voltage ride-through, low/high frequency ride-through, reactive power support, and other grid-assisting services [2, 3]. To meet these requirements, DG systems use power electronic inverters with fast and robust control capabilities, where the controller plays a role in ensuring accurate power regulation and maintaining stable operation under disturbances [4-6]. Currently, two main control methods are used, namely Proportional-Resonant (PR) control in the system (*αβ*) and Proportional-Integral (PI) control in the system (*dq*), which are equivalent in terms of basic components and are widely applied [7, 8]. In particular, single-phase grid-connected inverters play an important role thanks to their ability to provide high power quality and bidirectional power transmission. In addition to control strategies, inverter topology and modulation schemes, such as transformerless configurations designed to reduce leakage current and harmonic distortion, also significantly affect system performance [9-11]. In this work, a control strategy based on the (*d/q*) reference frame is applied, in which the *α/β–d/q* transformation converts sinusoidal signals into quasi-DC form, simplifying the design and increasing robustness against grid frequency changes. As a result, the PI controller can be used to achieve fast and stable performance, while allowing independent adjustment of active and reactive power through the *d*- and *q*-axis current components. Although derived from a three-phase system, this method has been effectively extended to single-phase inverters through appropriate signal generation and transformation techniques [12, 13].

To meet the high-performance requirements of single-phase grid-connected inverters, many control methods have been proposed [14]. PI controllers are simple but difficult to eliminate steady-state deviations [15], whereas PR control achieves zero deviation at the resonant frequency but is sensitive to grid frequency deviations [16]. Model Predictive Controllers (MPCs) offer fast response and good constraint handling, but are model-dependent and have high computational complexity [17, 18]. In general, these methods often have to compromise between accuracy, responsiveness, durability, and simplicity.

As an alternative, Sliding Mode Controllers (SMCs) are of interest due to their high durability, fast response, and good noise immunity [19, 20]. However, traditional SMCs suffer from chattering, and chattering reduction methods often have to compromise on switching frequency variation or degradation of durability and accuracy [21]. To further enhance robustness against uncertainties and disturbances, observer-based SMC approaches have been widely investigated [22]. Conventional observers, such as Luenberger observers and Extended Kalman Filters (EKFs), have been applied to estimate system states and lumped disturbances. Nevertheless, Luenberger observers rely heavily on accurate system models and may experience performance degradation under parameter variations, whereas EKF-based methods require prior knowledge of noise statistics and involve relatively high computational complexity, limiting their practical implementation in real-time inverter systems.

In this context, data-driven approximation techniques have attracted increasing attention [23]. Compared with conventional neural networks and fuzzy logic systems, Radial Basis Function (RBF) neural networks provide a simple structure with strong local approximation capability and more scalable computational complexity. In particular, unlike fuzzy systems that may suffer from rule explosion as the number of inputs increases, RBF networks maintain a more manageable computational burden, making them suitable for real-time control in power electronic systems.

Motivated by these observations, this paper proposes a model-free advanced SMC for single-phase grid-connected inverters by integrating an RBF neural network to estimate and compensate for uncertainties online, enhancing robustness and tracking while reducing chattering. The main contributions of the paper are summarized as follows:

- Enhanced uncertainty and disturbance compensation: Unlike the PI-based approach in [15], whose disturbance rejection capability strongly depends on fixed controller parameters, the proposed RBF neural network adaptively estimates and compensates for lumped uncertainties and external disturbances without requiring precise system knowledge, thereby improving robustness and current tracking performance.
- Finite-time Super-Twisting Sliding Mode Control (STSMC) with reduced chattering: In contrast to the traditional SMC method in [20], which suffers from severe chattering, the proposed STSMC achieves finite-time convergence with a continuous control signal, significantly reducing chattering while maintaining strong robustness against disturbances.
- Improved robustness and reduced conservatism: By integrating the RBF neural network with STSMC, the proposed controller reduces the reliance on large switching gains commonly required in conventional SMC approaches.

II. PROBLEM FORMULATION

A typical single-phase grid-connected inverter system, as shown in Figure 1, includes four main components: a DC power source v_{dc}, a power inverter, an Inductor-Capacitor-Inductor (LCL) filter, and the grid.

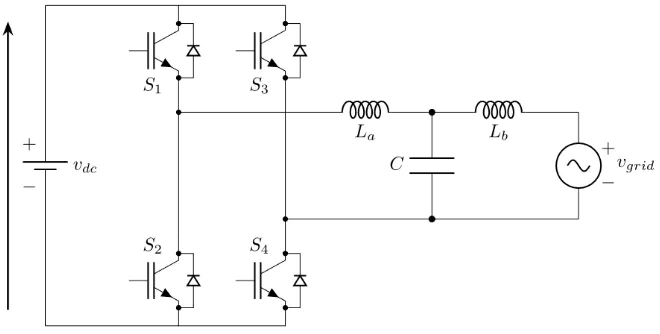

Fig. 1. Single-phase grid-connected inverter system with an LCL filter.

A. DC Power Source and Inverter

The DC source supplies a stable input to the H-bridge inverter, which uses Pulse Width Modulation (PWM) to generate an AC voltage $v_{inv}(t)$ with the required frequency and amplitude for grid injection.

B. Inductor-Capacitor-Inductor (LCL) Filter

The parameters of the LCL filter for a single-phase grid-connected inverter, as shown in Figure 2, are selected based on the following criteria: $THD < 5\%$; $Q_C \leq 0.1S$; $\Delta V_L \leq 0.1V_{rated}$; and $10f_g < f_r < 0.5f_{sw}$. Based on these, the system parameters are chosen as listed in Table I [1].

In the fundamental frequency range, the LCL filter can be assumed as a series of RL elements with equivalent parameters: $L_f = L_a + L_b$, $R_f = R_a + R_b$. Then, the filter's state equation is described by:

$$L_f \frac{di}{dt} + R_f i = v_{inv} - v_{grid} \tag{1}$$

where i_{grid} is the current pumped into the grid, v_{inv} is the voltage across the inverter, and v_{grid} is the grid voltage.

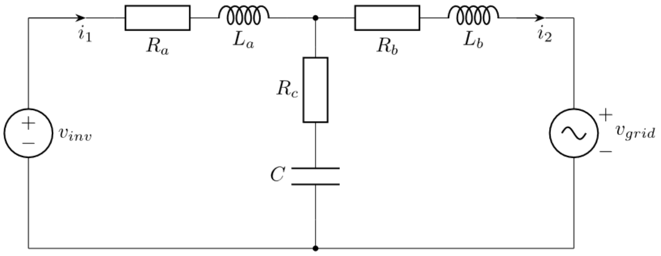

Fig. 2. LCL filter.

TABLE I. SYSTEM PARAMETERS

Parameters	Definition	Values
v_{dc}	Input DC voltage	400 DC
v_{grid}	Grid AC voltage	312 V
P_r	Rated power	2 kVA
f_g	Grid frequency	50 Hz
f_{sw}	Switching frequency	10 kHz
L_a	Inverter inductance	4.06 mH
L_b	Grid inductance	4.35 mH
C	Filter capacitance	500 μF
R_a, R_b, R_c	Resistance	0.001 Ω

C. *Power Grid and Synchronization Requirements*

The grid is modeled as an AC source:

$$v_{grid} = V_{grid}\sin\left(\mathrm{w}t + \phi_{grid}\right) \tag{2}$$

where w is the nominal angular frequency of the grid, and $\theta_{grid} = \mathrm{w}t + \phi_{grid}$ is the instantaneous phase of the grid voltage. In a *d/q* rotating system, the inverter needs to accurately estimate θ_{grid} to correctly transform the coordinates, ensuring that the current pumped into the grid is in phase and meets power quality standards.

III. CONTROL SUBSYSTEM

The grid-connected inverter control system is based on a current-control structure in the synchronous reference frame (*dq*0), as shown in Figure 3. The system consists of two main blocks: the Phase-Locked Loop (PLL) and the current control loop. Voltage and current signals are processed through an Orthogonal Signal Generator (OSG) and axis transformations to serve the control and generate PWM pulses.

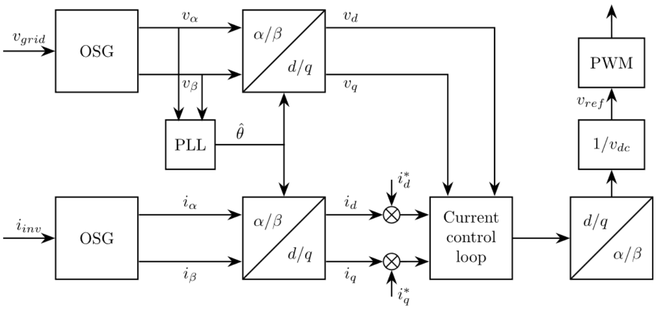

Fig. 3. Control subsystem.

A. *Phase-Locked Loop (PLL)*

For single-phase grid-tied inverters, PLLs are used to estimate the grid voltage phase angle and generate a reference signal for current control. The PLL structure [2], as shown in Figure 4, consists of the following components: an OSG that generates the signal pair (v_α, v_β), an axis transform block for acquisition (v_d, v_q), a PI controller for v_q error handling and generation $\hat{\mathrm{w}}$, and an angle updating integral block $\hat{\theta}$. In principle, the PLL is a closed-loop system that aligns the *d/q* system according to the grid voltage vector. After the OSG and axis converter, the voltage is separated into v_d and v_q; where v_q acts as the phase difference. When the PLL locks the phase, the angle is updated so that $v_q \to 0$.

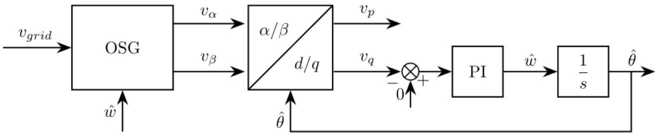

Fig. 4. PLL model.

1) *Orthogonal Signal Generator (OSG)*

In this study, the OSG was built based on a Modified First-Order Orthogonal Signal Generator (MFO-OSG), as shown in Figure 5 [4].

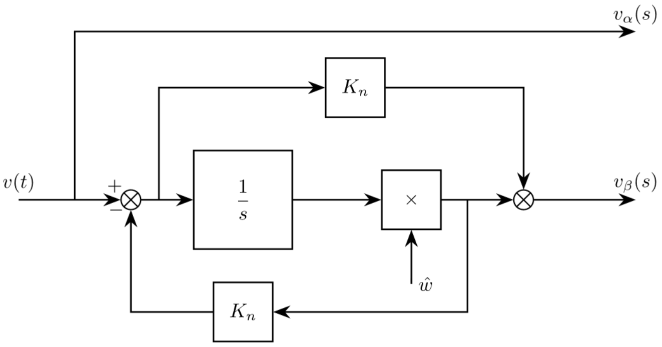

Fig. 5. MFO-OSG model.

Considering the single-phase grid voltage signal $v(t)$, the axis component α is determined directly as follows:

$$v_\alpha(s) = v(s) \tag{3}$$

Orthogonal components v_β are generated through an MFO filter with the transfer function:

$$v_\beta(s) = \frac{-K_n s + \hat{\mathrm{w}}}{s + K_n \hat{\mathrm{w}}} v(s) \tag{4}$$

where $\hat{\mathrm{w}}$ is the estimated angular frequency of the grid, and K_n is the filter adjustment parameter. When the estimated frequency $\hat{\mathrm{w}}$ coincides with the grid's fundamental frequency, the signal pair (v_α, v_β) has the same amplitude and frequency, and is phase-shifted by π/2, meeting the requirements of the OSG. In the proposed structure, the signals are used to perform synchronous coordinate transformations, thereby constructing a current control loop along the *d/q* axes. The use of the MFO-OSG allows for the creation of orthogonal signals with a simple structure and easy implementation in a digital control system.

2) Axis Transformation

The signal v_α is mapped onto the *d*-axis and used as the outer control loop to regulate the active power. The signal v_β corresponds to the *q*-axis, controlling the reactive power. According to the DQ frame theory, the active and reactive current components are determined as follows [3]:

$$\begin{bmatrix} v_d \\ v_q \end{bmatrix} = \begin{bmatrix} \cos(\hat{\theta}) & \sin(\hat{\theta}) \\ -\sin(\hat{\theta}) & \cos(\hat{\theta}) \end{bmatrix} \begin{bmatrix} v_\alpha \\ v_\beta \end{bmatrix} \tag{5}$$

where v_d and v_q are the direct and quadrature axis grid side current, respectively; $\hat{\theta}$ is the estimated angular from PLL.

IV. CURRENT CONTROL LOOP

In single-phase grid-tied inverters, LCL filters are widely used to attenuate harmonics; however, their inherent high-frequency resonance and parameter variations may affect system stability. In this study, since the LCL filter is considered within the control design through an equivalent RL approximation, the unmodeled resonance dynamics are treated as lumped uncertainties. To address these issues, a model-independent current control strategy is proposed by integrating an RBF neural network with STSMC. The RBF network enables online estimation and compensation of uncertainties, whereas STSMC provides a continuous control signal that reduces high-frequency switching effects. As a result, the proposed approach enhances robustness, mitigates resonance excitation, and ensures stable operation under parameter variations.

Applying the axis transformation (6), the current model of the LCL filter in the *d/q* axes has the form:

$$\begin{cases} L_f \dfrac{di_d}{dt} + R_f i_d - \mathrm{w} L_f i_q = v_{inv,d} - v_{grid,d} \\ L_f \dfrac{di_q}{dt} + R_f i_q + \mathrm{w} L_f i_d = v_{inv,q} - v_{grid,q} \end{cases} \tag{6}$$

The goal of the current control loop is to determine the appropriate reference voltages applied to the inverter $v^*_{inv,d}$ and $v^*_{inv,q}$ on the *d* and *q* axes. From these components, the reference voltage vector V_{ref} is synthesized and fed into the PWM modulation block, thereby adjusting the inverter's output voltage to ensure that the grid-connected current follows the reference signal.

Let $x_1 = i_d$, $x_2 = i_q$, $u_1 = v_{inv,d} - v_{grid,d}$, and $u_2 = v_{inv,q} - v_{grid,q}$, the system (6) becomes:

$$\begin{cases} L_f \dot{x}_1 + R_f x_1 - \mathrm{w} L_f x_2 = u_1 \\ L_f \dot{x}_2 + R_f x_2 + \mathrm{w} L_f x_1 = u_2 \end{cases} \tag{7}$$

In practical operation, the parameters of this filter L_f and R_f are often not fixed and may differ from the nominal model; therefore, the filter model (7) is rewritten as follows:

$$\begin{cases} L\dot{x}_1 + d_1 = u_1 \\ L\dot{x}_2 + d_2 = u_2 \end{cases} \tag{8}$$

where $d_1 = (L_f - L)\dot{x}_1 + R_f x_1 - \mathrm{w} L_f x_2$ and $d_2 = (L_f - L)\dot{x}_2 + R_f x_2 + \mathrm{w} L_f x_1$ are total uncertainties, and L and R are the predefined values of L_f and R_f.

Set $e_1 = i_d - i_d^* = x_1 - x_1^*$ and $e_2 = i_q - i_q^* = x_2 - x_2^*$ are current errors on *d/q* axes, the sliding surfaces are chosen as:

$$s_i = e_i + \lambda_i \int_0^t e_i d\tau,\ i = 1,2 \tag{9}$$

Combining (8) and (9), the derivatives of the sliding surfaces are given by:

$$\begin{aligned} L\dot{s}_i &= L\dot{x}_i - L\dot{x}_i^* + L\lambda_i e_i \\ &= u_i - d_i - L\dot{x}_i^* + L\lambda_i e_i,\ i = 1,2 \end{aligned} \tag{10}$$

A. Traditional Sliding Model Control (TSMC)

For traditional sliding mode control, the control signals are designed as follows:

$$u_i = L\dot{x}_i^* - L\lambda_i e_i - k_i \operatorname{sgn}(s_i),\ i = 1,2 \tag{11}$$

Applying to (10), we have:

$$L\dot{s}_i = -d_i - k_i \operatorname{sgn}(s_i),\ i = 1,2 \tag{12}$$

Then the Lyapunov candidate function is chosen as:

$$V_{TSMC} = \frac{1}{2}Ls_1^2 + \frac{1}{2}Ls_2^2 \geq 0 \tag{13}$$

The derivative of the Lyapunov function is determined by:

$$\dot{V}_{TSMC} = -s_1(d_1 + k_1 \operatorname{sgn}(s_1)) - s_2(d_2 + k_2 \operatorname{sgn}(s_2)) \tag{14}$$

In order to $\dot{V}_{TSMC} \leq 0$, the control gain k_1 and k_2 must be positive and sufficiently large to satisfy $k_1 > |d_1|$ and $k_2 > |d_2|$.

Traditional SMCs are favored for their simple structure and good noise resistance. With a sufficiently large switching coefficient, the system achieves fast convergence and tracks the sliding surface. However, it is difficult to precisely determine the noise limit, often leading to the selection of an excessively large coefficient, causing chattering; conversely, if chosen with a small coefficient, the sliding conditions are not guaranteed, reducing performance or causing instability.

B. Advanced Sliding Model Control (ASMC) Based on Radial Basis Function (RBF)

To overcome the chattering and switching coefficient dependence on traditional SMCs, this study uses STSMC to ensure finite convergence with a continuous signal, significantly reducing chattering. Besides, an integrated RBF network is used to estimate uncertainty, reduce conservatism in parameter selection, and improve system robustness.

1) Super-Twisting Sliding Mode Control (STSMC) Design

The sliding mode control law is designed using a super-twisting structure as follows:

$$u_i = u_{eqi} + u_{rbfi} + u_{swi},\ i = 1,2 \tag{15}$$

where the equivalent component u_{eqi} is:

$$u_{eqi} = L\dot{x}_i^* - L\lambda_i e_i,\ i = 1,2 \tag{16}$$

and the super-twisting component u_{swi} [6] is given by:

$$\begin{aligned} u_{swi} &= -k_{i1}|s_i|^{\frac{1}{2}} sgn(s_i) + v_i, \\ \dot{v}_i &= -\frac{1}{2}k_{i2} sgn(s_i),\ \ i = 1,2 \end{aligned} \tag{17}$$

with $k_{i1}, k_{i2} > 0,\ i = 1,2$. Finally, the RBF component u_{rbfi} is designed as:

$$u_{rbfi} = \hat{d}_i,\ i = 1,2 \tag{18}$$

where $\hat{d}_i,\ i = 1,2$ are the estimated values of the uncertainties d_i, which are designed in the following section. The STSMC algorithm guarantees that the sliding variable and its derivative converge to zero within a finite time interval with a continuous control signal, thereby significantly decreasing chattering compared to traditional SMCs.

2) Uncertainty Estimation Using Radial Basis Function (RBF) Neural Network

Because the uncertainty components $d_i,\ i = 1,2$ are unknown beforehand, an RBF neural network is used to approximate these values:

$$d_i = \mathbf{W}_i^{*T}\boldsymbol{\varphi}(\mathbf{x}_i),\ i = 1,2 \tag{19}$$

where $\mathbf{W}_i^* \in \mathbb{R}^{n\times 1}$ is the ideal weight vector, and $\boldsymbol{\varphi}(\mathbf{x}_i) = [\varphi_1(\mathbf{x}_i), \varphi_2(\mathbf{x}_i), \cdots, \varphi_n(\mathbf{x}_i)]^T \in \mathbb{R}^{n\times 1}$ is the Gaussian basis function vector given by:

$$\varphi_j(\mathbf{x}_i) = \exp\left(\frac{\|\mathbf{x}_i - \mathbf{c}_j\|}{2b_j^2}\right),\ j = 1 \div n \tag{20}$$

where $\mathbf{x}_i = \left[e_1, e_2, \int_0^t e_1 d\tau, \int_0^t e_2 d\tau\right]^T$ are the input vectors; n is the number of hidden nodes; and $\mathbf{c}_j$ and b_j are the centroid vector and width of each hidden node, respectively. The estimated uncertain component is:

$$\hat{d}_i = \hat{\mathbf{W}}_i^T\boldsymbol{\varphi}(\mathbf{x}_i),\ i = 1,2 \tag{21}$$

$$\dot{\hat{\mathbf{W}}}_i = -\frac{1}{2}|s_i|^{\frac{1}{2}}\left(\mu L\frac{L + k_{i2}}{2k_{i1}}|s_i|^{\frac{1}{2}}\mathrm{sgn}(s_i) - \frac{1}{2}\mu v_i\right)\boldsymbol{\varphi}(\mathbf{x}_i) \tag{22}$$

where $\mu > 0$. The use of RBF networks enables real-time estimation and compensation of uncertainty, thereby reducing the residual noise amplitude that affects the sliding mode controller and easing the burden of selecting gain parameters.

Remark 1: For the RBF network, the centers $\mathbf{c}_j$ are selected to be uniformly distributed across the expected operating ranges of the inputs, whereas the widths b_j are set proportional to the spacing between adjacent centers. The number of hidden nodes n is chosen to balance approximation accuracy and computational efficiency.

3) Closed-Loop Stability

Theorem 1: Consider the closed-loop control system (8) and the STSMC control law (15) combined with the proposed RBF neural network (19)–(21). Then, with appropriately selected control parameters $k_{i1}, k_{i2} > 0,\ i = 1,2$ and adaptive gain $\mu > 0$, the sliding variables s_i and their derivatives $\dot{s}_i$ will converge to a small neighborhood around the origin.

Proof: Combining (15)–(22), we have:

$$L\dot{s}_i = -k_{i1}|s_i|^{\frac{1}{2}} sgn(s_i) + v_i - \tilde{\mathbf{W}}_i^T\boldsymbol{\varphi}(\mathbf{x}_i) \tag{23}$$

with $\tilde{\mathbf{W}}_i = \mathbf{W}_i^* - \hat{\mathbf{W}}_i$. Defining the auxiliary state vectors:

$$\boldsymbol{\xi}_i = \left[L|s_i|^{\frac{1}{2}} sgn(s_i), v_i\right]^T,\ i = 1,2 \tag{24}$$

Then, with $\mathbf{A}_i = \begin{bmatrix} \frac{-k_{i1}}{L} & 1 \\ \frac{-k_{i2}}{L} & 0 \end{bmatrix}$ and $\mathbf{B}_i = \left[-\tilde{\mathbf{W}}_i^T\boldsymbol{\varphi}(\mathbf{x}_i) \quad 0\right]^T$, $i = 1,2$, the derivatives of $\boldsymbol{\xi}_i,\ i = 1,2$ have the form:

$$\dot{\boldsymbol{\xi}}_i = \left[\frac{1}{2}L|s_i|^{-\frac{1}{2}}\dot{s}_i,\ \dot{v}_i\right]^T = \frac{1}{2}|s_i|^{-\frac{1}{2}}\mathbf{A}_i\boldsymbol{\xi}_i + \frac{1}{2}|s_i|^{-\frac{1}{2}}\mathbf{B}_i \tag{25}$$

The Lyapunov candidate function is chosen as follows:

$$V_i = \frac{1}{2}\boldsymbol{\xi}_i^T\mathbf{P}_i\boldsymbol{\xi}_i + \frac{1}{2}\tilde{\mathbf{W}}_i^T\tilde{\mathbf{W}}_i \geq 0,\ i = 1,2 \tag{26}$$

where $\mathbf{P}_i = \mu\begin{bmatrix} \frac{L + k_{i2}}{2k_{i1}} & -\frac{1}{2} \\ -\frac{1}{2} & \frac{L^2 + Lk_{i2} + k_{i1}^2}{2k_{i1}k_{i2}} \end{bmatrix}$ are positive definite symmetric matrices. Then, with $\mathbf{I}$ being the identity matrix, we have:

$$\mathbf{A}_i^T\mathbf{P}_i + \mathbf{P}_i\mathbf{A}_i = \begin{bmatrix} -\mu & 0 \\ 0 & -\mu \end{bmatrix} = -\mu\mathbf{I} \tag{27}$$

The derivatives of the Lyapunov functions are given by:

$$\dot{V}_i = \frac{1}{2}\dot{\xi}_i^T \mathbf{P}_i \xi_i + \frac{1}{2}\xi_i^T \mathbf{P}_i \dot{\xi}_i + \tilde{\mathbf{W}}_i^T \dot{\tilde{\mathbf{W}}}_i = -\frac{1}{4}\left|s_i\right|^{-\frac{1}{2}} \xi_i^T \mu \mathbf{I} \xi_i \le 0 \quad (28)$$

Based on Babarlat's lemma, the sliding surfaces will be practically stable and converge to a small neighborhood around the origin. Hence, Theorem 1 is proven.

Remark 2: In this structure, the RBF network functions as an approximation and compensates for the uncertain component, reducing conservatism in the selection of coefficients k_1 and k_2, while the STSMC guarantees the existence of sliding mode and finite-time system stability. This combination limits chattering, thereby minimizing the excitation of high-frequency resonant modes of the LCL filter, making the proposed control method more suitable for real-world inverter systems.

V. SIMULATION RESULTS AND DISCUSSION

This section presents simulation results evaluating the proposed controller for a single-phase grid-tied inverter. All simulations are conducted in MATLAB/Simulink over a 0.3 s time window, and the results are benchmarked against the PI controller presented in [15] and the TSMC controller proposed in [20], with control parameters listed in Table II.

TABLE II. CONTROL PARAMETERS

Controller	**Parameters**
Proposed	$\lambda_1 = \lambda_2 = 3$ (9), $k_{11} = 150$, $k_{12} = 100$, $k_{21} = k_{22} = 100$ (17), $b_j = 2$, $n = 5$, $c_j \in \{-1; -0.5; 0; 0.5; 1\}$ (20), $\mu = 500$ (22)
TSMC	$\lambda_1 = \lambda_2 = 3$ (9), $k_1 = k_2 = 200$ (11)
PI	$k_p = 250.1$, $k_i = 0.5022$

Two simulation cases are conducted to comprehensively evaluate controller performance: Case 1 focuses on ideal conditions to assess dynamic response and decoupling capability, whereas Case 2 targets robustness under realistic hardware deployment with combined model uncertainties and grid disturbances:

- Case 1: Model-in-the-Loop (MIL): The controller and plant are both simulated in MATLAB/Simulink under nominal model conditions. This case evaluates the dynamic response and channel decoupling capability of the proposed controller; the *d*- and *q*-axis reference currents step from −10 A to 10 A at $t = 0.15$ s.
- Case 2: Processor-in-the-Loop (PIL): The controller is cross-compiled and executed on a TI C2000 F28377S microcontroller, whereas the plant model continues to run in MATLAB/Simulink, with data exchanged between the hardware and the host PC, as shown in Figure 6. This case introduces simultaneous model parameter deviations and non-ideal grid conditions to evaluate tracking capability and robustness under realistic deployment constraints. Specifically, the filter resistance is increased by a factor of 5 and the grid-side inductance is increased by a factor of 3; in addition, the grid voltage is subjected to a 20% voltage sag superimposed with a 3% fifth-order harmonic component. The *q*-axis reference current i_q^* steps from 0 to 10 A at $t = 0.15$ s, whereas the *d*-axis reference i_d^* is held at 0 A to maintain a unity power factor condition.

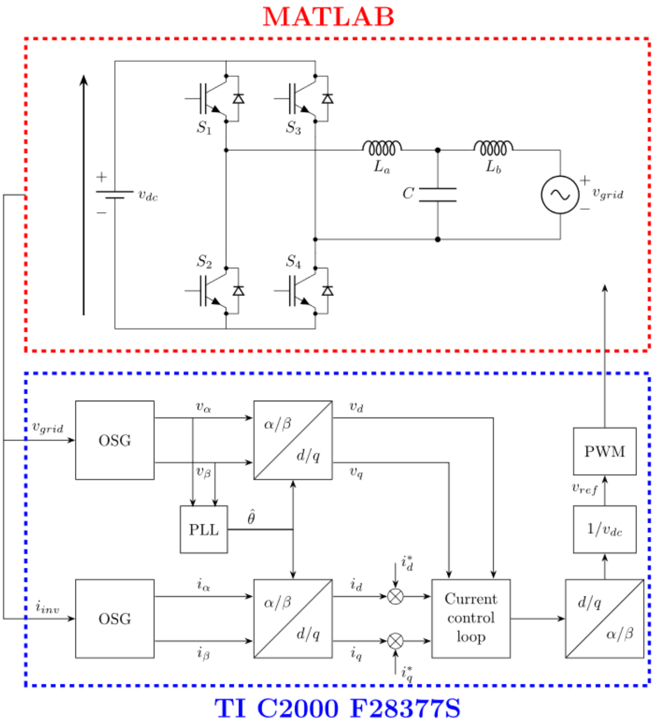

Fig. 6. PIL block diagram of the control system.

A. *Case 1: Model-in-the-Loop (MIL)*

This case evaluates the dynamic response of current control loops under nominal model conditions. Simulation results show significant differences in tracking capability and transient characteristics between the three methods. Figure 7 shows that the proposed controller achieves a fast response, small overshoot, and near-zero steady-state error, whereas the PI controller has the largest overshoot and the TSMC controller responds more slowly.

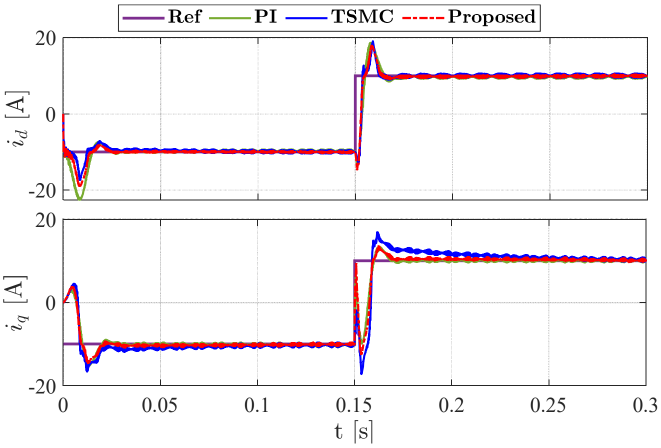

Fig. 7. Current values in the *d/q* axes in Case 1.

Figure 8 illustrates the grid current, where the proposed method maintains stable amplitude and frequency with small oscillations, whereas the PI and TSMC controllers exhibit more pronounced oscillations; in particular, the TSMC controller exhibits high-frequency oscillations during the transient phase due to chattering.

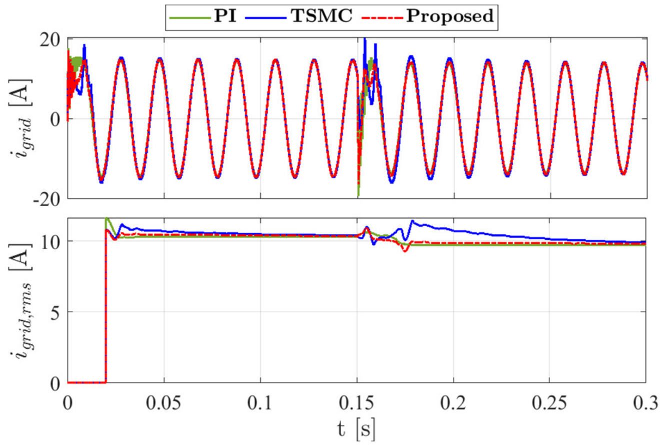

Fig. 8. Grid current in Case 1.

Figure 9 shows that the grid voltage and RMS values remain stable with a sinusoidal waveform, almost unaffected by the change in reference current at $t = 0.15$ s, confirming that the proposed method does not degrade voltage quality.

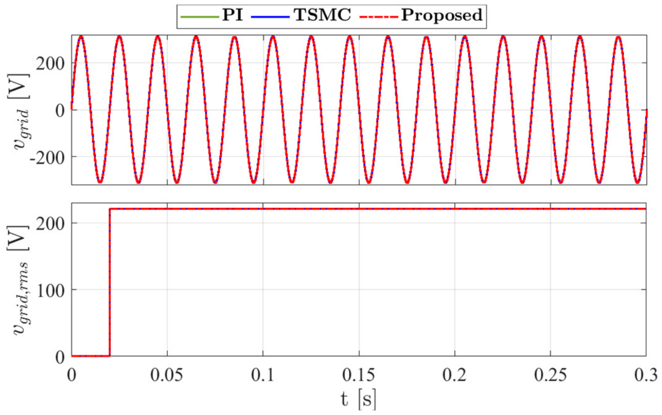

Fig. 9. Grid voltage in Case 1.

Figure 10 presents the power response, where PI causes a slight overshoot in active power P, whereas TSMC causes an overshoot in reactive power Q. Conversely, the proposed method maintains both P and Q within rated limits with smaller fluctuations, indicating more stable operating characteristics.

Figure 11 shows that the proposed method achieved lower and more stable Total Harmonic Distortion (THD) compared to other methods; whereas TSMC exhibited high-frequency THD fluctuations, and PI maintained a higher THD level throughout the simulation.

B. Case 2: Processor-in-the-Loop (PIL)

This case is selected as the main scenario to evaluate the controller's robustness under both model mismatch and non-ideal grid conditions. The controller algorithm is cross-compiled and deployed on a TI C2000 F28377S microcontroller, whereas the plant model runs in MATLAB/Simulink, enabling verification of the algorithm's implementability on the target embedded processor.

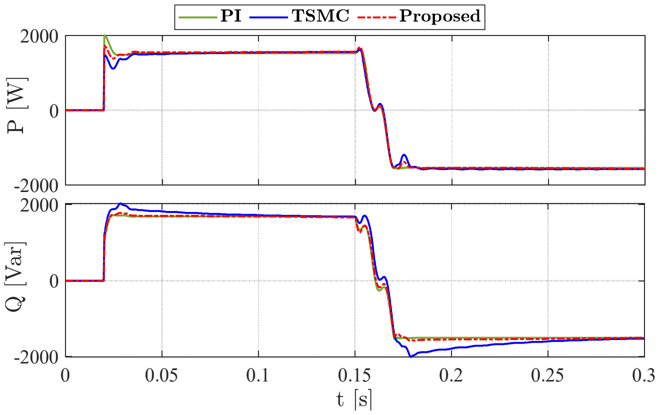

Fig. 10. Active and reactive power in Case 1.

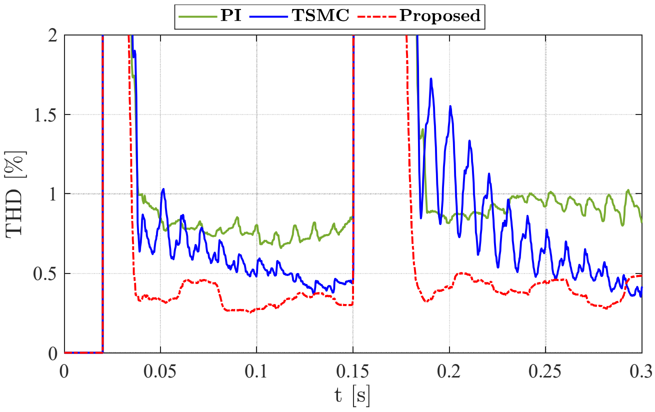

Fig. 11. THD values in Case 1.

Specifically, the filter resistance is increased by a factor of 5 and the grid-side inductance is increased by a factor of 3; in addition, the grid voltage is subjected to a 20% voltage sag superimposed with a 3% fifth-order harmonic component, as shown in Figure 12.

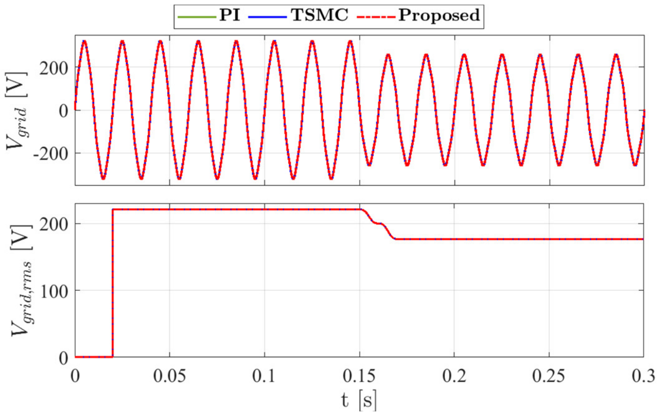

Fig. 12. Grid voltage in Case 2.

The *q*-axis reference current i_q^* steps from 0 to 10 A at t = 0.15 s, whereas the *d*-axis reference i_d^* is held at 0 A to maintain a unity power factor condition.

As shown in Figure 13, the proposed controller maintains fast convergence, small overshoot, and near-zero steady-state error in both *d*- and *q*-axis currents despite the combined disturbances, confirming that the algorithm operates correctly when executed on the embedded hardware. In contrast, the PI controller exhibits the largest overshoot during the transient, whereas the TSMC controller shows more pronounced oscillations and a longer settling time.

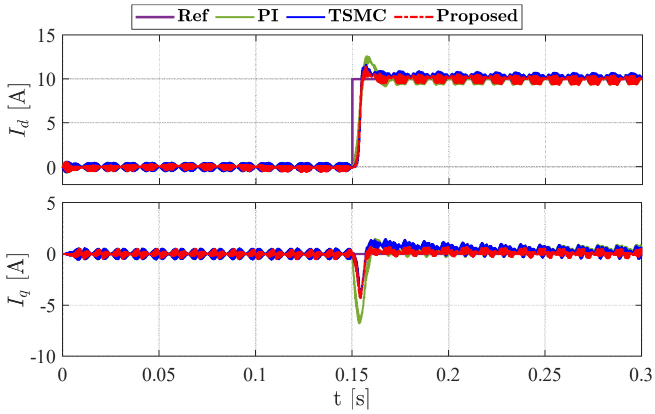

Fig. 13. Current values in *d*/*q* axes in Case 2.

The grid current response in Figure 14 confirms that the proposed method preserves a smoother sinusoidal waveform and a more stable RMS transition under distorted grid conditions. Although the injected voltage harmonic and sag degrade the current quality in all cases, the proposed controller suppresses the resulting oscillations more effectively than PI and TSMC, indicating stronger disturbance rejection capability.

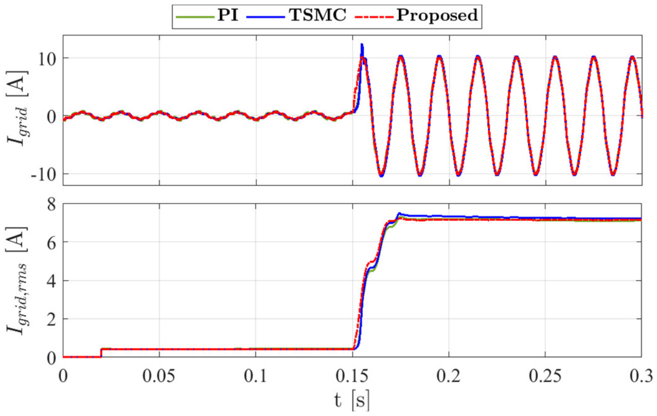

Fig. 14. Grid current in Case 2.

The power results in Figure 15 indicate that the active power is accurately tracked, whereas the reactive power remains approximately zero, consistent with the unity power factor operating condition.

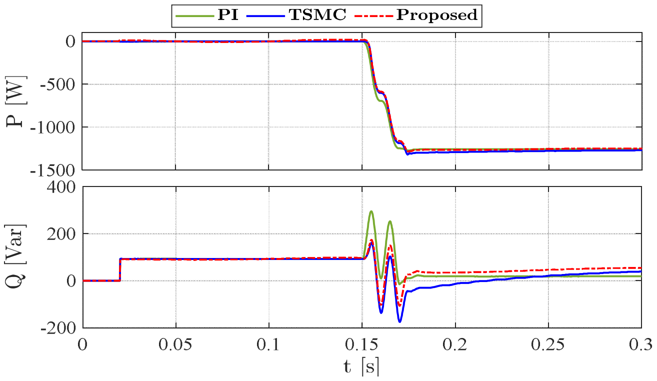

Fig. 15. Active and reactive power in Case 2.

Regarding current quality, Figure 16 shows that the current THD increases under non-ideal grid conditions due to the injected harmonic distortion and voltage sag. Nevertheless, the proposed method maintains the lowest and most stable THD, remaining under 4%, whereas PI and TSMC (approximately 5%) exhibit higher distortion and larger residual oscillations.

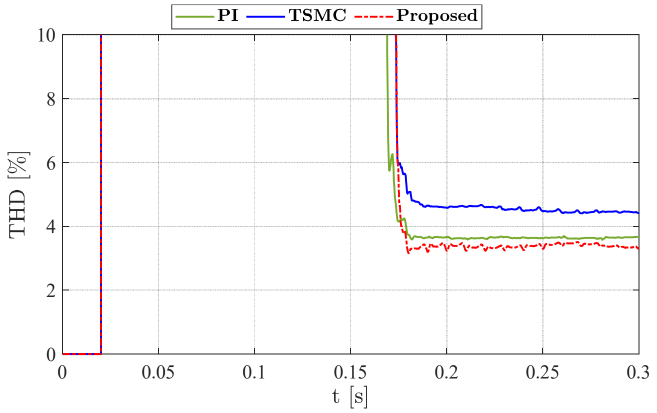

Fig. 16. THD values in Case 2.

These results confirm that the proposed controller effectively mitigates the impact of distorted grid voltage and preserves robust current quality, while the PIL setup further validates that the algorithm can be correctly compiled and executed on the TI C2000 F28377S processor.

C. Quantitative Comparison

Table III provides a quantitative comparison of average THD, steady-state time, and overshoot for all controllers in both simulation scenarios. In Case 1, the proposed method achieved the lowest average THD (0.4041%) and the fastest steady-state time in both current channels, whereas PI produced the highest THD and TSMC showed the slowest convergence, especially in the i_q channel (almost 5 times slower than the other two).

In Case 2, under combined conditions of model error and non-ideal grid conditions, the average THD increased for all methods, but the proposed controller still achieved the lowest value (3.3831%) and the fastest steady-state time. It also produced the smallest overshoot in the i_d channel while maintaining competitive performance in the i_q channel.

Overall, the proposed RBF–STSMC provides the best balance between dynamic response and steady-state performance.

TABLE III. QUANTITATIVE PERFORMANCE COMPARISON

Case	Controller	THD (%)	Settling time (s)		Overshoot (A)	
			i_d	i_q	i_d	i_q
Case 1	Proposed	0.4041	0.0189	0.0187	8.15	3.67
	TSMC	0.6703	0.0190	0.0986	9.10	6.87
	PI	0.9223	0.0239	0.0192	8.63	3.43
Case 2	Proposed	3.3831	0.0083	0.0152	1.47	4.32
	TSMC	4.5155	0.0647	0.1056	1.64	4.37
	PI	3.6370	0.0174	0.0178	2.58	6.77

D. Discussion

The superior performance of the proposed RBF–STSMC can be explained from both control structure and physical perspectives. Compared with conventional SMC, the use of the super-twisting algorithm generates a continuous control signal, which significantly reduces high-frequency switching components and chattering. This effect can be observed in smoother control response and reduced oscillations in the current waveform, as shown in Figures 8 and 14.

In addition, the integration of the RBF neural network enables online estimation of lumped uncertainties, including parameter variations and unmodeled dynamics. As a result, the controller can adapt during transient conditions, leading to faster convergence and improved tracking accuracy. This explains the reduced settling time, overshoot, and lower THD observed in the proposed method, as presented in Table III.

Beyond control performance, the PIL simulation in Case 2 provides an additional layer of validation by confirming that the proposed algorithm can be successfully cross-compiled and executed on the TI C2000 F28377S embedded processor without functional degradation. The consistency between the PIL results and the MIL results in Case 1 indicates that the algorithm is numerically well-conditioned and compatible with fixed-point or floating-point arithmetic constraints of the target hardware, supporting its feasibility for embedded implementation.

Overall, the combination of reduced chattering, adaptive uncertainty compensation, and verified embedded deployability allows the proposed controller to achieve both improved dynamic response and enhanced steady-state performance compared to PI and conventional SMC methods, even under non-ideal grid conditions.

VI. CONCLUSION

This paper proposes an advanced current control strategy for a single-phase grid-connected inverter under conditions of parameter uncertainty and disturbance. The method combines Super-Twisting Sliding Mode Control (STSMC) with a Radial Basis Function (RBF) neural network observer, ensuring finite-time convergence, reducing chattering, and improving robustness against unmodeled parameter variations and dynamic deviations.

Thanks to the uncertainty compensation mechanism, the proposed method also reduces conservatism in gain selection and improves tracking performance under varying operating conditions. Lyapunov stability analysis demonstrates the stability of the closed-loop system, while simulation results show fast transient response, high accuracy, and reduced jitter compared to traditional SMC and PID methods.

Future research will focus on experimental validation using Hardware-in-the-Loop (HIL) testing, where both the controller and the plant are implemented on dedicated real-time hardware platforms to enable closed-loop verification under realistic timing constraints before physical prototype deployment. Beyond HIL validation, the work will be extended to multi-phase inverters and microgrids with parallel converters, where coupling effects and coordination among multiple units require further investigation. Addressing these issues, particularly the scalability of RBF-based observers and the robustness of STSMC under coupling dynamics, will be a key direction for future work.

DECLARATION OF COMPETING INTERESTS

Not applicable to this work

ACKNOWLEDGMENT

Not applicable to this work

DATA AVAILABILITY

Data availability is not applicable to this paper, as no new data were created or analyzed in this study.

REFERENCES

[1] G. Spagnuolo, "Smart Solar PV Inverters with Advanced Grid Support Functionalities [Book News]," *IEEE Industrial Electronics Magazine*, vol. 17, no. 1, pp. 109–110, Mar. 2023, https://doi.org/10.1109/MIE.2023.3235600.

[2] Y. Yang, S. Bremner, C. Menictas, and M. Kay, "Modelling and optimal energy management for battery energy storage systems in renewable

energy systems: A review," *Renewable and Sustainable Energy Reviews*, vol. 167, Oct. 2022, Art. no. 112671, https://doi.org/10.1016/j.rser.2022.112671.

[3] M. Shirkhani *et al.*, "A review on microgrid decentralized energy/voltage control structures and methods," *Energy Reports*, vol. 10, pp. 368–380, Nov. 2023, https://doi.org/10.1016/j.egyr.2023.06.022.

[4] M. Malengret and C. T. Gaunt, "Active Currents, Power Factor, and Apparent Power for Practical Power Delivery Systems," *IEEE Access*, vol. 8, pp. 133095–133113, 2020, https://doi.org/10.1109/ACCESS.2020.3010638.

[5] M. K. Ikram, M. S. J. Asghar, M. Seyedmahmoudian, S. Mekhlilef, A. Stojcevski, and A. Al-Assaf, "Advanced real and reactive power measurement using analog multiplier and phase-controlled switching technique," *Sensors and Actuators A: Physical*, vol. 378, Nov. 2024, Art. no. 115812, https://doi.org/10.1016/j.sna.2024.115812.

[6] H. I. Hazim, K. A. Baharin, C. K. Gan, A. H. Sabry, and A. J. Humaidi, "Review on Optimization Techniques of PV/Inverter Ratio for Grid-Tie PV Systems," *Applied Sciences*, vol. 13, no. 5, Mar. 2023, Art. no. 3155, https://doi.org/10.3390/app13053155.

[7] D. Li, T. Wang, W. Pan, X. Ding, and J. Gong, "A comprehensive review of improving power quality using active power filters," *Electric Power Systems Research*, vol. 199, Oct. 2021, Art. no. 107389, https://doi.org/10.1016/j.epsr.2021.107389.

[8] C. Zou, B. Liu, S. Duan, and R. Li, "Stationary Frame Equivalent Model of Proportional-Integral Controller in dq Synchronous Frame," *IEEE Transactions on Power Electronics*, vol. 29, no. 9, pp. 4461–4465, Sept. 2014, https://doi.org/10.1109/TPEL.2013.2296789.

[9] M. Kwon, S. Park, C. Oh, J. Lee, and S. Choi, "Unified Control Scheme of Grid-Connected Inverters for Autonomous and Smooth Transfer to Stand-Alone Mode," *IEEE Transactions on Power Electronics*, vol. 37, no. 1, pp. 416–425, Jan. 2022, https://doi.org/10.1109/TPEL.2021.3102151.

[10] K. Zeb *et al.*, "A Review on Recent Advances and Future Trends of Transformerless Inverter Structures for Single-Phase Grid-Connected Photovoltaic Systems," *Energies*, vol. 11, no. 8, July 2018, Art. no. 1968, https://doi.org/10.3390/en11081968.

[11] A. H. Sabry, Z. M. Mohammed, F. H. Nordin, N. H. Nik Ali, and A. S. Al-Ogaili, "Single-Phase Grid-Tied Transformerless Inverter of Zero Leakage Current for PV System," *IEEE Access*, vol. 8, pp. 4361–4371, 2020, https://doi.org/10.1109/ACCESS.2019.2963284.

[12] M. Monfared, S. Golestan, and J. M. Guerrero, "Analysis, Design, and Experimental Verification of a Synchronous Reference Frame Voltage Control for Single-Phase Inverters," *IEEE Transactions on Industrial Electronics*, vol. 61, no. 1, pp. 258–269, Jan. 2014, https://doi.org/10.1109/TIE.2013.2238878.

[13] R. Panigrahi, S. K. Mishra, S. C. Srivastava, A. K. Srivastava, and N. N. Schulz, "Grid Integration of Small-Scale Photovoltaic Systems in Secondary Distribution Network—A Review," *IEEE Transactions on Industry Applications*, vol. 56, no. 3, pp. 3178–3195, May 2020, https://doi.org/10.1109/TIA.2020.2979789.

[14] H. Eroğlu, E. Cuce, P. Mert Cuce, F. Gul, and A. Iskenderoğlu, "Harmonic problems in renewable and sustainable energy systems: A comprehensive review," *Sustainable Energy Technologies and Assessments*, vol. 48, Dec. 2021, Art. no. 101566, https://doi.org/10.1016/j.seta.2021.101566.

[15] M. Waqas *et al.*, "DQ Transformation Based Control of Single-Phase Grid-Tied Inverter," in *2021 31st Australasian Universities Power Engineering Conference*, Perth, Australia, 2021, pp. 1–6, https://doi.org/10.1109/AUPEC52110.2021.9597712.

[16] G. Shen, X. Zhu, J. Zhang, and D. Xu, "A New Feedback Method for PR Current Control of LCL-Filter-Based Grid-Connected Inverter," *IEEE Transactions on Industrial Electronics*, vol. 57, no. 6, pp. 2033–2041, June 2010, https://doi.org/10.1109/TIE.2010.2040552.

[17] J. Hu, Y. Shan, J. M. Guerrero, A. Ioinovici, K. W. Chan, and J. Rodriguez, "Model predictive control of microgrids – An overview," *Renewable and Sustainable Energy Reviews*, vol. 136, Feb. 2021, Art. no. 110422, https://doi.org/10.1016/j.rser.2020.110422.

[18] R. Aljarrah, B. B. Fawaz, Q. Salem, M. Karimi, H. Marzooghi, and R. Azizipanah-Abarghooee, "Issues and Challenges of Grid-Following Converters Interfacing Renewable Energy Sources in Low Inertia Systems: A Review," *IEEE Access*, vol. 12, pp. 5534–5561, 2024, https://doi.org/10.1109/ACCESS.2024.3349630.

[19] L. Wu, J. Liu, S. Vazquez, and S. K. Mazumder, "Sliding Mode Control in Power Converters and Drives: A Review," *IEEE/CAA Journal of Automatica Sinica*, vol. 9, no. 3, pp. 392–406, Mar. 2022, https://doi.org/10.1109/JAS.2021.1004380.

[20] D. G. Montoya, C. A. Ramos-Paja, and R. Giral, "Improved Design of Sliding-Mode Controllers Based on the Requirements of MPPT Techniques," *IEEE Transactions on Power Electronics*, vol. 31, no. 1, pp. 235–247, Jan. 2016, https://doi.org/10.1109/TPEL.2015.2397831.

[21] H. Komurcugil, S. Biricik, S. Bayhan, and Z. Zhang, "Sliding Mode Control: Overview of Its Applications in Power Converters," *IEEE Industrial Electronics Magazine*, vol. 15, no. 1, pp. 40–49, Mar. 2021, https://doi.org/10.1109/MIE.2020.2986165.

[22] Q. Teng, G. Xu, X. Zheng, H. Mai, X. Ma, and Y. Wang, "A novel sliding mode observer-based compound sliding mode current control with active damping for single phase grid-tied inverter system in weak grid," *International Journal of Electrical Power & Energy Systems*, vol. 141, Oct. 2022, Art. no. 108117, https://doi.org/10.1016/j.ijepes.2022.108117.

[23] V.-Q. Nguyen and T.-L. Le, "Flexible Control with Fuzzy Observer-Based Sliding mode for Multilevel Inverter," *Journal of Electrical Engineering & Technology*, vol. 19, no. 7, pp. 4573–4586, Sept. 2024, https://doi.org/10.1007/s42835-024-01878-9.